




Optimization of magnetic properties of BaTiO₃/Li_{0.5}Fe_{2.5}O₄ multiferroics prepared via modified low-temperature combustion

N. G. Imam^{1,*} , Mennatallah AbouHasswa², Ahmed I. Ali^{3,4}, and N. Okasha²

¹Experimental Nuclear Physics Department (Solid State Lab.), Nuclear Research Center (NRC), Egyptian Atomic Energy Authority (EAEA), Cairo 13759, Egypt

²Physics Department, Faculty of Girls, Ain Shams University, Cairo 11722, Egypt

³Basic Science Department, Faculty of Technology and Education, Helwan University, Sray El-Quba, Cairo 11281, Egypt

⁴Nanotechnology Research Center, British University in Egypt (BUE), Elshrok-city, Cairo 11837, Egypt

Received: 25 October 2021

Accepted: 14 February 2022

Published online:

9 March 2022

© The Author(s) 2022

ABSTRACT

Multiferroic $(x)\text{BaTiO}_3/(1-x)\text{Li}_{0.5}\text{Fe}_{2.5}\text{O}_4$ ($0.0 \leq x \leq 1$) perovskite/spinel nanocomposite was synthesized using a modified citrate auto-combustion method. Both BaTiO₃ (BTO) and Li_{0.5}Fe_{2.5}O₄ (LFO) phases along with their composites were successfully characterized using X-ray diffraction, Fourier transformation infrared spectroscopy, and X-ray absorption fine structure spectroscopy. The nanoscale, morphology, and magnetic properties were imaged and acquired using high resolution transmission electron microscopy, atomic force microscopy, and vibrating sample magnetometer. Synchrotron radiation-based elemental selective XAFS technique was performed around Fe *K*-edge to obtain the selective and the detailed local structural information of Li_{0.5}Fe_{2.5}O₄ nanoparticles (NPs). The main remarkable result in this work is the enhancement in the coercivity (H_C) of LFO NPs after compositing with BTO particularly at $x = 0.6$, and at $x = 0.8$. Based on the collected results, BTO/LFO nanocomposite can be seen as a good candidate for different technological applications including magnetically modulated piezoelectric, safety rechargeable batteries, and multilayer ceramic capacitor.

1 Introduction

Tailoring and controlling the composite materials properties are the key in the advanced modern and future technology that meets the human needs and

ambitions especially in solving the energy and environment crises [1]. Composite is a tailored controlled material system which consists of two or more distinguished separate phases [2]. The aim of the nanocomposite fabrication is to get a new advanced

Address correspondence to E-mail: nama_emam@yahoo.com

material system with novel characteristics and highly efficient performance. Accordingly, the main advantage of composites is the ability to tailor new materials with new properties for modern applications. Basically, the output new composite properties depend on the different own physicals and chemical features of the original constituent phases [3]. Furthermore, nanocomposite is a subset of composites that takes the advantage of the unique materials properties on the small scale (at which at least one of its constituents is in nanoscale) [4]. Composites usually have three parts; namely, a matrix, structural constituents and an the hetero-interface [5]. The matrix is a homogeneous phase which surrounds the other phases (fillers), and the hetero-interface which is the boundary area among the different phases and the matrix network. With the development of electronic technology, composite materials have been widely used for electronic devices where higher densities, limited space and multifunction are required [6]. On the other hand, multiferroic nanocomposite is an important class of nanocomposite that have become in attention because of their promising applications such as in energy conversion, fuel cells, storage, shape memory actuation and solid-state refrigeration, next-generation spintronics devices or multiple state memory elements, and transducers with magnetically modulated piezoelectricity [1–7]. In particular, biferroic is a class of multiferroics that shows the simultaneous ferroelectric and ferromagnetic order parameters [8]. Generally, the concept of multiferroic stands for the presence of an interaction between the ferroelectric and ferromagnetic subsystems. That is, the external electric field affects the magnetic properties, and vice versa; the magnetic field affects the electric polarization [3]. It was reported that, it is not easy to design a single-phase material that shows the coexisting of both ferroelectric and ferromagnetic ordering at room temperature [3]. Therefore, the ferroelectric/ferrite composite is considered as a good solution for the material system that gives the multiferroic (magnetoelectric) properties [1–5]. Lithium ferrite is an inverse spinel crystal structure, where three fifths of the Fe^{3+} cations (1.5) and Li^{1+} cations are supposed to be octahedrally coordinated in B site (octahedral) sublattice. Lithium ferrite is a good candidate in numerous technological applications such as in safety rechargeable batteries, because it possesses high resistivity, low dielectric loss at high frequencies and high Curie point [9]. The

second phase in the composite (Barium titanate) is reported as a very important ferroelectric material due to its eco-friendly ferroelectric character; free from toxics for the environment [10]. Barium titanate (BTO) is a perovskite type oxide group which is the most popular ferroelectric material used in multi-layer ceramic capacitors, piezoelectric and positive temperature coefficient devices [10]. The ferroelectric behavior of BTO is arising from the crystal asymmetry which is associated with the displacement of Ti ion from its body-centered positions in the crystal lattice [11, 12]. Zheng et al. reported that BTO NPs can enhance the multifunctional properties of $\text{Li}_{0.5}\text{Fe}_{2.5}\text{O}_4$ [8].

One important point here to be mentioned is that, this work is a completion of our previously published work by Imam et al. [2]; that focused on the systematic study of the dielectric properties of BTO/LFO nanocomposite. The $(x)\text{BTO}/(1-x)\text{LFO}$ composites have been synthesized by a modified citrate precursor auto combustion method and characterized using XRD and Near Edge XAFS (XANES) to investigate the average and electronic structural. The Synchrotron based XAFS technique is an important technique for probing the electronic/local structure of the material, even for more diluted and disordered nanomaterials and multicomponent materials such as nanocomposites [13–15].

In this work, the XAFS technique was utilized in order to probe the own atomic/local structure of Lithium ferrite at Fe *K*-edge before incorporating it in the target LFO/BTO nanocomposite. The XAFS spectrum consists of two portions namely, XANES or X-ray absorption near edge structure spectroscopy and EXAFS or Extended X-ray absorption fine structure spectroscopy [14]. Generally, XANES gives detailed information about the electronic and oxidation states of the absorbing ions and provides details about the site symmetry and local coordination chemistry around the absorber [2, 15]. While EXAFS is a brilliant synchrotron technique mapping the fine atomic environment surrounding the absorber ion in the media. Moreover, EXAFS images the induced local distortions around the target selective ion upon doping with impurities. Furthermore, bond length R , mean-square relative displacement σ^2 , and coordination numbers N of the coordination shells around the selective target absorbing ion are the main output structural parameters from the EXAFS fitting [16]. The local/atomic structure in addition the cation site

occupancy influence strongly on the magnetic properties. From the EXAFS fitted bond distance, the cation distribution between the sublattices of the spinel structure can be identified [13–16].

In this contribution, we intended to study the magnetic properties of the target composite and linked the observed magnetic behavior with the own fine structure of the magnetic phase and the weight percent of the BTO phase. Consequently, the main aim of this work is to focus on the optimization of the magnetic properties of $\text{BaTiO}_3/\text{Li}_{0.5}\text{Fe}_{2.5}\text{O}_4$ multiferroics prepared via modified relatively low-temperature combustion technique. The prepared $(x)\text{BaTiO}_3/(1-x)\text{Li}_{0.5}\text{Fe}_{2.5}\text{O}_4$ nanocomposites ($x = 0, 0.2, 0.4, 0.6, 0.8$ and 1) were characterized using various experimental techniques such as FTIR, HRTEM, AFM, and SR-XAFS. The main originality of this work lies in exploring the role of the chemical, fine/electronic, and imaging properties on the magnetic performance of $(x)\text{BaTiO}_3/(1-x)\text{Li}_{0.5}\text{Fe}_{2.5}\text{O}_4$ nanocomposites.

2 Experimental procedures: materials and methods

Nanocomposite with the nominal composition of $(x)\text{BTO}/(1-x)\text{LFO}$ with $x = 0, 0.2, 0.4, 0.6, 0.8,$ and 1.0 were synthesized by the modified citrate precursor auto combustion method. The details of the synthesis process of BTO and LFO were described previously in the flowchart mapped in our published paper by Imam et al. [2]. While Fig. 1 shows the coupling between $(x)\text{BaTiO}_3$ and $(1-x)\text{Li}_{0.5}\text{Fe}_{2.5}\text{O}_4$ at $x = 0.0, 0.2, 0.4, 0.8,$ and 1.0 . In addition, the crystal structure of the multiferroic composite and their constituent phases were determined by X-ray diffractometer [Proker D_8 model with CuK_α radiation ($\lambda = 1.5418 \text{ \AA}$)] in a wide range of Bragg's angle (2θ) ranging from 10° to 70° at room temperature. The XRD results were published in our paper [2]. Herein we recall the XRD results to confirm the formation of the nanocomposite without any extra phases. Also, the XRD results were combined with those of the local structure which were extracted from the XAFS spectra in order to explain the magnetic behavior of LFO in the target composite.

Transmission electron microscope (HRTEM, JEOL-1010) was used to image the morphology (particle shape and size) of the samples. The infrared spectra

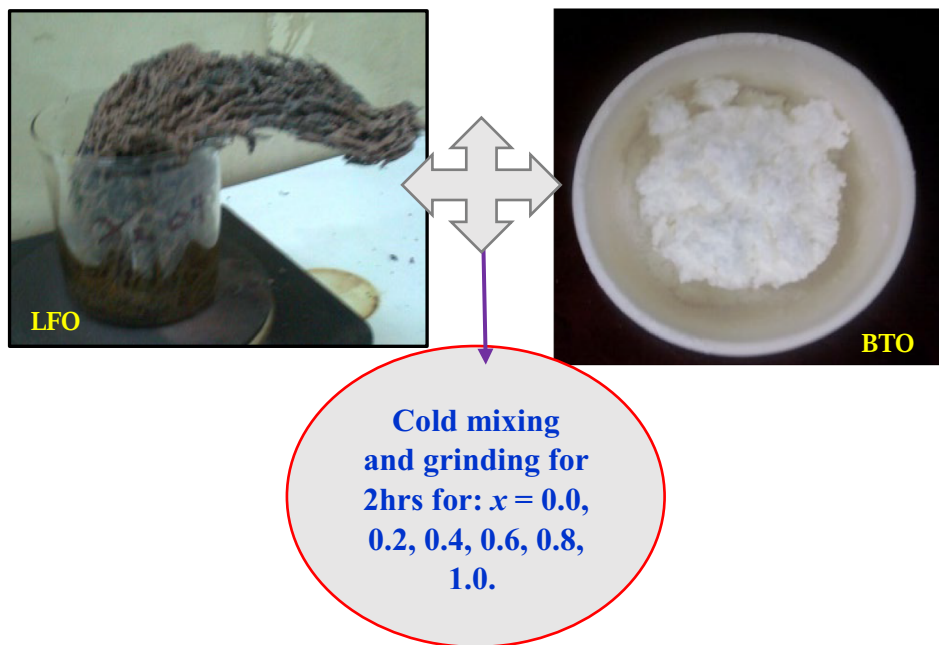
(FTIR) of the investigated samples recorded (IR spectrometer model FT/IR-6100) in the range from 4000 to 400 cm^{-1} using KBr matrix. FTIR was used to provide information about the chemical/bond nature of the coupling between LFO and BTO nanoparticles. The atomic force microscopy (AFM Agilent 5500) is used for characterizing nanocomposites of $(x)\text{BaTiO}_3$ and $(1-x)\text{Li}_{0.5}\text{Fe}_{2.5}\text{O}_4$ at $x = 0.0, 0.2, 0.4, 0.8,$ and 1.0 . It determines size, morphology, surface texture and roughness [17–19].

The measurement of the magnetic susceptibility was performed using Faraday's method [20] at different temperatures ranging from 300 to 1023 K as a function of different applied magnetic field intensities of ($1010, 1340,$ and 1660 Oe). The temperature of the samples was measured using K -type thermocouple with a junction very closed to the sample keeping it free. The accuracy of magnetic susceptibility measurements was $\pm 1\%$.

The magnetic parameters were extracted from the analysis of the collected $M-H$ hysteresis loops. Vibrating sample magnetometer (VSM; Lake Shore - 7410-USA) with a maximum applied magnetic field of $\pm 20 \text{ kOe}$ was employed [20].

The Italian 11.1 XAFS beamline of Elettra synchrotron radiation source in Trieste-Italy was used for XAFS data collection around 7112 keV of Fe K -edge [21]. The sample was finely powdered and composited into polyvinyl pyrrolidone (PVP) matrix and then pressed into pellet with a diameter of 13 mm and with a proper highly uniform optical thickness. XAFS data collection of both $\text{Li}_{0.5}\text{Fe}_{2.5}\text{O}_4/\text{PVP}$ sample and the reference of iron foil were simultaneously measured in the transmission mode and at room temperature (295 K). Four scans were acquired, merging, and averaging to assure the spectral reproducibility. The extended XAFS (EXAFS) data was reduced using the Demeter-0.9.26 package standard procedures (version 0.9.26, Naval Research Laboratory, Washington, DC, 20375, USA) [22, 23]. Fits of the k^2 weighted EXAFS data were carried out in R space using theoretical functions from the FEFF9 code. High-quality k -space data were obtained up to 12 \AA^{-1} and the full fit range was $1.00\text{--}3.7 \text{ \AA}$ (R -space). The refined input fitting EXAFS parameters were the amplitude reduction factor S_0^2 , mean-square relative displacement σ^2 , the interatomic bond lengths R , the absorption edge energy shift between the sample and the theoretical model ΔE_0 . The refinement of the relative contribution of tetrahedral

Fig. 1 Coupling between $(1 - x)$ $\text{Li}_{0.5}\text{Fe}_{2.5}\text{O}_4$ and $(x)\text{BaTiO}_3$; ($x = 0.0, 0.2, 0.4, 0.8,$ and 1.0)



and octahedral site-occupancy for the Fe ions was also included in the EXAFS fitting analysis [13].

3 Results and discussion

3.1 Average crystal, chemical, and morphological structural analyses

The detailed study of the average crystal structure of for $(x)\text{BTO}/(1 - x)$ LFO nanocomposite was essentially described in our previously published paper [2]. The XRD patterns confirmed the formation of $(x)\text{BTO}/(1 - x)\text{LFO}$ nanocomposites with the two discrete original constituent phases without the appearance of any secondary/impurity extra phases. The average crystallite size of $(x)\text{BTO}/(1 - x)$ LFO composite was around 55 ± 5 nm.

Figure 2 shows the acquired FTIR spectra of BTO/LFO nanocomposites in the absorption mode. The main absorption FTIR peak positions are tabulated in Table 1. The functional groups corresponding to the FTIR spectra peak of the two composite phases are marked as shown in Fig. 2. The apparent FTIR absorption peaks support the XRD results, described in [2], and confirm the successful formation of the only two distinguished separate phases with a high crystalline quality and free of secondary phases.

Figure 3 illustrated the typical HRTEM morphology. The micrographs indicated the nanostructure

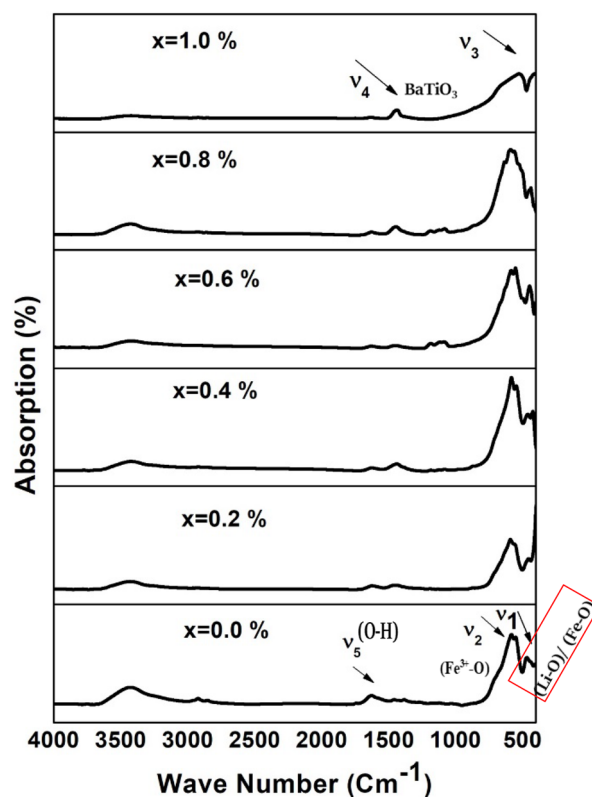


Fig. 2 FTIR spectra of BTO/LFO nanocomposites in the absorption mode at different x ($x = 0.0, 0.2, 0.4, 0.8,$ and 1.0)

nature with the spherical like shape at $x = 0$. While the HRTEM image exhibits rod-like morphology for BTO ($x = 1.0$) with a length of 120 nm and a diameter

Table 1 FTIR absorption bands in (cm⁻¹) for (x)BTO/(1 - x)LFO

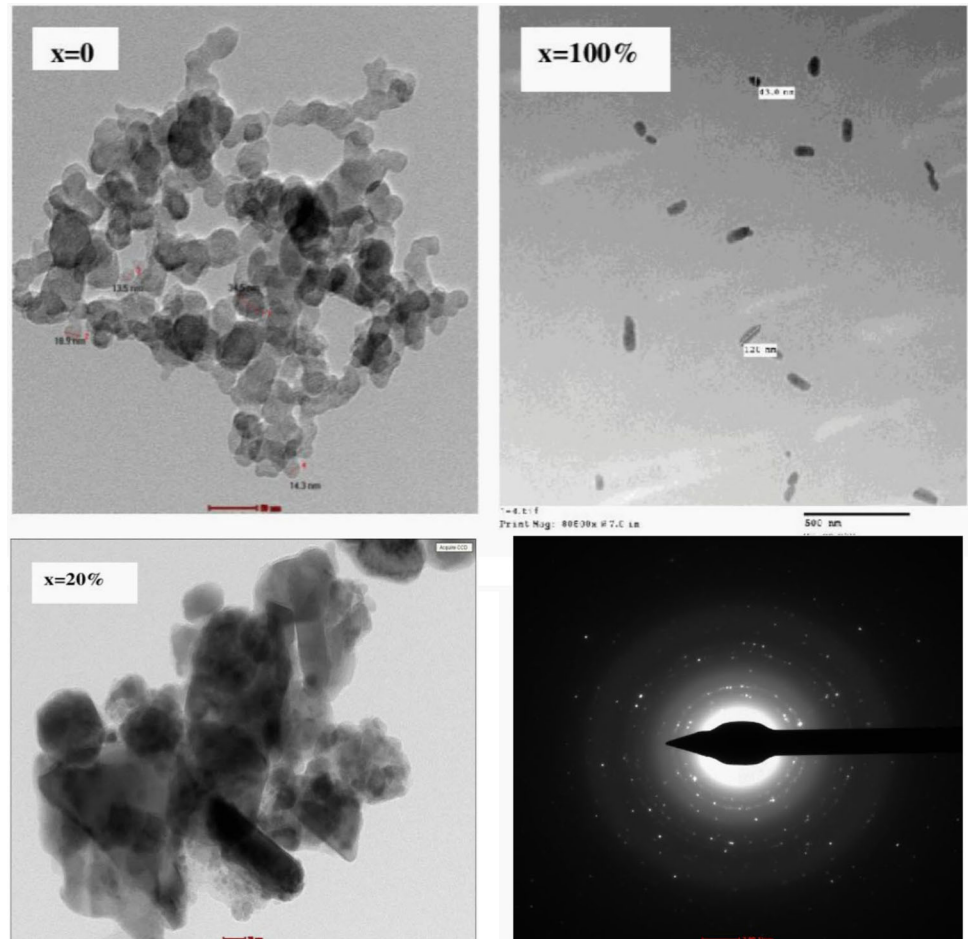
x	Tetrahedral (A-site) Fe ³⁺ -O (v ₂)	Octahedral (B-site) Li-O(v ₁)/Fe-O	BaTiO ₃		Adsorbed moisture (O-H)	
			(v ₃)	(v ₄)	(v ₅)	(v ₆)
0.0	583	467	–	–	1627	3426
0.2	583	467	527	1437	1627	3426
0.4	583	467	527	1437	1627	3426
0.6	583	467	527	1437	1627	3426
0.8	583	467	527	1437	1627	3426
1.0	–	–	527	1437	1627	3426

of 43 nm. HRTEM images prove that the modified citrate auto-combustion method was a successful and facile method for obtaining nanorod-like shape of the perovskite material (BTO). The average crystallite size of the BTO NPs obtained from X-ray diffraction was around 47 nm [2]. The selected area electron diffraction (SAED) pattern of the sample with x = 0.2 is shown in the inset of Fig. 3. The bright, sharp, and ordered rings show the polycrystalline nature of the sample, and each ring refers to a specific crystal plane

of the polycrystalline material. The existence of the two different spots at each ring represents the diffraction from the two different constituent phases within the composite. The reciprocal of the distance between the two successive rings gives the value of the d spacing.

It is known that the AFM topographic image of the sample is obtained by plotting the deflection of the cantilever versus its position on the sample surface. Alternatively, it is possible to plot the height position

Fig. 3 TEM morphology of BTO/LFO multiferroics, and the SAED of HRTEM



of the translation stage. This height is controlled by a feedback loop, which maintains a constant force between the tip and the sample.

Figure 4a, b shows the surface AFM topography and the average roughness (R_a) of the BaTiO₃ sample of ($R_a \simeq 29.3$ nm). The contrast in the AFM image arises from the dependence of the force between the tip and the sample on both tip–sample separation and the own properties of both the tip and the sample [24]. The graph shows that the grain size of BaTiO₃ is $\simeq 59.1$ nm, confirming the polycrystalline structure in the BaTiO₃ grains.

3.2 Local/atomic structural study: XAFS analysis

The Fe *K*-edge XAFS technique was accessed to describe the local geometry and electronic structure of/around Fe absorbing atom in the LFO phase. The Fe *K*-edge XANES probes the unoccupied 4p orbitals with $1s \rightarrow 4p$ dipole transitions and unoccupied 3d orbitals via the much weaker intensity pre-edge, $1s \rightarrow 3d$, transitions. While the Fe *K*-edge EXAFS quantifies the interference effects due to electron scattering from the surrounding ions.

The local/atomic structure is necessary for explaining and understanding the magnetic behavior of Li_{0.5}Fe_{2.5}O₄ NPs. Accordingly, EXAFS study is a useful technique for imaging the fine local structure in a short-range order surrounding the absorbing ions (up to 5 Å). The normalized Fe *K*-edge absorption full XAFS spectrum ($\mu(E)$) obtained for Li_{0.5}-Fe_{2.5}O₄ NPs is plotted and presented in Fig. 5. As aforementioned above, the XAFS data was collected at room temperature (295 K) in the transmission geometry. The XAFS spectrum shows three different energy regions with respect to the main maximum peak or the white-line position. These three regions include the pre-edge energy region that is before the main absorption edge (around 7114.44 ± 0.04 eV). Second, the main absorption edge which could be selected differently. The red circle in the normalized XAFS spectrum represents the main absorption edge opted position in the half-height of the edge step. The pre-edge plus the main absorption edge, in addition to the white-line (maximum intensity peak) are described as the near edge XAFS (XANES) region or the X-ray absorption near edge spectroscopy which is a fingerprint characteristic feature (the inset of Fig. 5). The post-edge secondary peaks appeared a few 10 eV

above the main absorption edge are attributed to the multiple scattering from the surrounding back scatterers shells (Fe, Li, or/and oxygen ions). After the post edge, the oscillatory signal region is the extended X-ray absorption fine structure spectroscopy (EXAFS). These oscillations are expressed by an EXAFS equation reported in [25].

The oxidation state/s of Fe was/were identified from the first derivative of the XANES spectra ($d\mu(E)/dE$) and by comparing the peak positions and intensities of the sample spectrum along with those of the iron reference model compounds as shown in Fig. 6. The first derivative of the XANES spectrum gives a more resolved and distinguished peak position more than that in case of original XANES direct spectrum [13]. It is observed that the first inflection point corresponding to the pre-edge position of the LFO sample is very close to that of the Fe₂O₃ (Fe³⁺) reference compound, confirming the trivalent character of iron ions within the LFO NPs. Also, the second or the highest intensive inflection point corresponding to the main absorption edge or the maximum of the white-line position of LFO is almost coincident with that of Fe₂O₃ (Fe³⁺) spectrum, supporting the same result of the formation of Fe ions in the Fe³⁺ oxidation.

On the other hand, the extraction of the normalized EXAFS part of the XAFS spectrum multiplied by κ^2 is revealed in Fig. 7a. The well seen magnified EXAFS oscillations was taken up to $k \simeq 12 \text{ \AA}^{-1}$. FTs or Fourier transform amplitude of the k^2 weighted EXAFS signal is plotted in Fig. 7b, while the FTs envelope of the EXAFS oscillations is plotted in Fig. 7c. The variation in the amplitude of the FTs envelope indicates the different surround environments (back scatterers ions) around the absorbing ion. The FTs amplitude spectrum shows that the average Fe–O bond distance in the first coordination nearest neighbors is located around 1.477 \AA^{-1} . The second peak represents the Fe–Fe/Li bond lengths in the second coordination shell. It is clear that the second peak is splitting into two different distinguished peaks representing the Fe_B–Fe_B and Fe_B–Fe_A/Fe_A–Fe_A, respectively. This splitting confirms the distribution of Fe absorbing ions between the two tetrahedral and octahedral sublattices of the spinel structure shown in Fig. 7. The ratio between the FTs amplitude of the octahedral peak to that of the tetrahedral peak could be used to estimate the cation

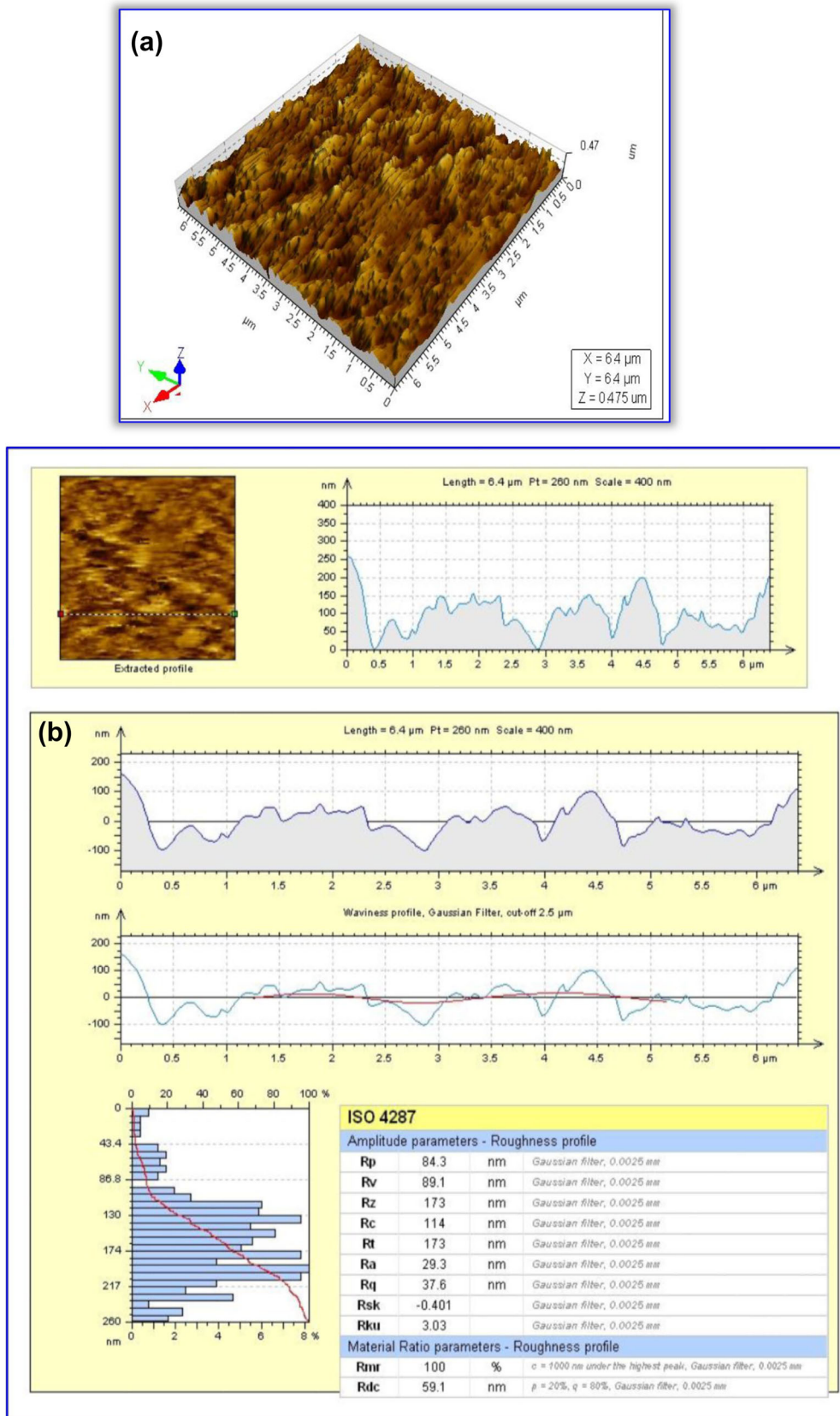


Fig. 4 a, b AFM image for BaTiO₃ nanomultiferroics showing the surface topography, grain shape and size

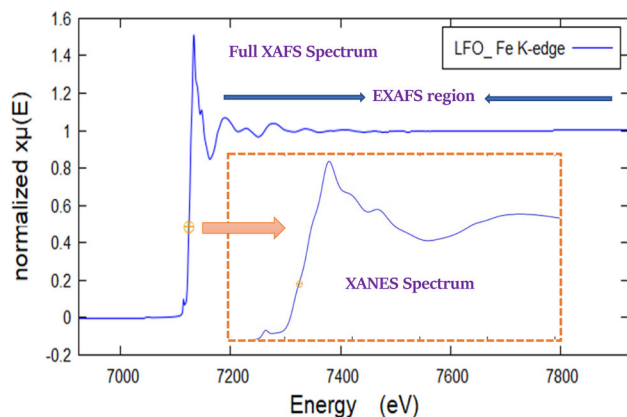


Fig. 5 Normalized full XAFS signal collected at Fe K-edge, the inset is the XANES region of the XAFS spectrum

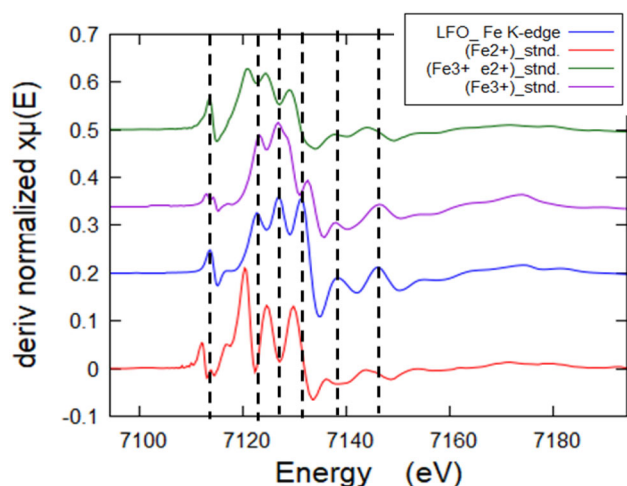


Fig. 6 First derivatives of XANES spectra of $\text{Li}_{0.5}\text{Fe}_{2.5}\text{O}_4$ along with those of iron standard compounds including different Fe oxidation states

distribution. Accordingly, it was found that the calculated cation distribution was as follow:



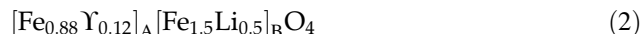
where, Y is the vacancy, representing the structure disorder that saturates the deficiency of Fe ions in tetrahedral site. The detected structure disorder from EXAFS analysis will affect the magnetic behavior as will be shown in the discussion of the magnetic properties.

Furthermore, and for determining the fine local structural parameters such as the near neighbor bond lengths of the Fe ions; the EXAFS spectrum was fitted using the theoretical structural model of $\text{Li}_{0.5}\text{Fe}_{2.5}\text{O}_4$ NPs (ICDD # 88-0671) [27]. Figure 8 explores the magnitude of FTs of EXAFS signal in k -range from 3

to 12 \AA , across Fe K-edge along with the respective best fit of $\text{Li}_{0.5}\text{Fe}_{2.5}\text{O}_4$ NPs. On the other words, Fig. 8 shows the comparison between the best-fit results and the collected EXAFS spectrum reported for the FTs magnitude and the imaginary part (Left Panel), and the extracted k^3 signal (Right Panel).

Table 2 listed the well-fit structural parameters of the nearest and next nearest coordination shells of $\text{Li}_{0.5}\text{Fe}_{2.5}\text{O}_4$ NPs. The R -Factor of the fit was in the value ≈ 0.02 and the overall reduction factor S_0^2 was fixed to be 1.00 for all the selected scattering paths and all coordination neighbors in order to reduce the correlations among the fitting parameters. Whereas only the single scattering paths (SSP) were considered during the EXAFS fit. The first peak around 2 \AA is corresponding to the two Fe–O bond lengths, which involves Fe_A –O (1.948 \AA) and Fe_B –O (2.121 \AA), as a reflection from the tetrahedral and octahedral site occupancy, respectively. The second splitting peak in the range of 2.5–4 \AA is arisen from the different possible contributions from the Fe_B – Fe_B (3.024 \AA)/ Fe_B – Li_B (3.143 \AA), Fe_A – Fe_A (3.486 \AA), and Fe_A – Fe_B (3.546 \AA) bonds. It is observed that the Mean Square Relative Displacement (σ^2) increases from 0.007 \AA^2 (for the first coordination shell) up to 0.040 \AA^2 (for the higher coordination shells). This increase is expected due to the larger disorder of the superficial shells.

The fitted inversion parameter (x), (representing the percentage % of the occupancy of the tetrahedral (A) and octahedral (B) sites by Fe^{3+} ions), has the value around 0.88. Consequently, the extracted cation site distribution is in this form of:



Where, Y is the vacancy representing the structure disorder that saturates the deficiency of Fe in the tetrahedral site, as mentioned above.

It is remarkable that the calculated and the extracted inversion parameter (x) and in turns the relevant cationic distributions, extracted directly from the collected EXAFS signal along with that extracted from the EXAFS fitting, are very close to each other.

3.3 Magnetic behavior of $(x)\text{BaTiO}_3/$ $(1-x)\text{Li}_{0.5}\text{Fe}_{2.5}\text{O}_4$ nanocomposite

Figure 9a shows the temperature dependence of the magnetic susceptibility (χ_M) for the investigated

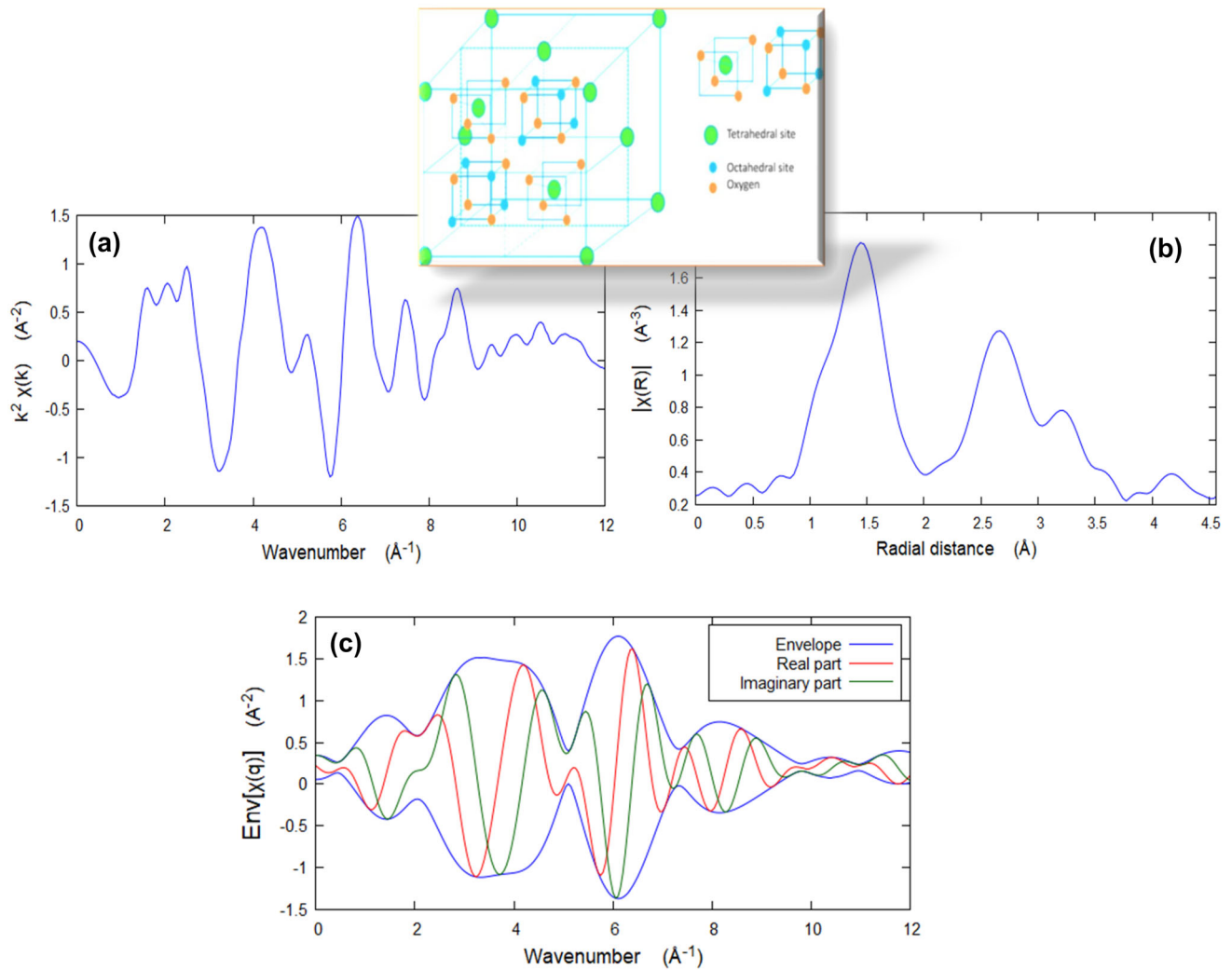


Fig. 7 **a** $k^2\chi(k)$ EXAFS oscillations. **b** Fourier transform (FT) magnitude corresponding to $k^2\chi(k)$ EXAFS signal, and **c** Envelope of EXAFS signal of real and imaginary parts in q -space. Schematic structure of the spinel ferrite [26]

nanocomposites at different magnetic field intensities. It is shown that, a normal ferrimagnetic character is the general trend for all the samples where χ_M decreases gradually with the temperature until reaching the Curie temperature (T_C), after above the sample gives the paramagnetic trend. The χ_M decreases with increasing the magnetic field intensity as $M = \chi_M * H$. By increasing the magnetic field intensity, the magnetization increases and χ_M decreases slightly going hand in hand to cause irreversible domain wall motion. Figure 9b shows the first derivative of the magnetization versus temperature curves for (x) BTO/ $(1 - x)$ LFO nanocomposites. Where the minimum point of the first derivative peak represents the Curie temperature (T_C) of the samples. It was observed that the Curie temperature was

decreased by increasing the BaTiO₃ content in the multiferroic except at $x = 0.6$; the T_C was enhanced.

Figure 10a shows the effect of BaTiO₃ content (x) on the effective magnetic moment (μ_{eff}), while Fig. 10b displays the effect of BaTiO₃ content (x) on the T_C (K) and χ_M at room temperature. The variation of the magnetic parameters such as Curie temperature (T_C), magnetic susceptibility (χ_M), and effective magnetic moment (μ_{eff}) as a function of BaTiO₃ content (x) in (x) BTO/ $(1 - x)$ LFO magnetoelectric nanocomposite at room temperature is listed in Table 3. The value of (μ_{eff}) increases with the increase in BTO content up to $x = 0.6$ then decreases. This trend is due to the presence of the non-magnetic perovskite phase and the hetero-interface effects, which influence the magnetic properties of the

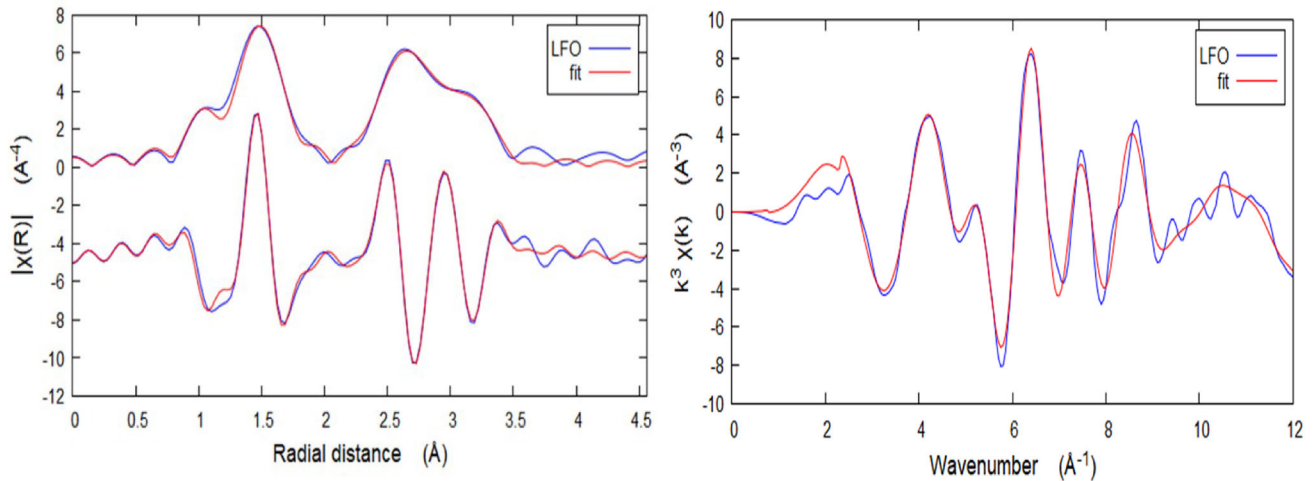


Fig. 8 Comparison between the best-fit results and the collected EXAFS spectrum. Comparisons are reported for the FT magnitude and imaginary part (Left Panel), and the extracted k^3 signal (Right Panel)

Table 2 Best-fit structural EXAFS parameters of the first and second coordination shells of $\text{Li}_{0.5}\text{Fe}_{2.5}\text{O}_4$; R -factor = 0.02 (2), and k -range = 3–12 at the Fe K -edge

Absorber-backscatter bond (shell)	$N \pm 0.1$	$\sigma^2(\text{\AA}^2) \pm 0.008$	$R (\text{\AA}) \pm 0.015$
$\text{Fe}_B\text{-O}$ (1st shell)	6.0	0.007	2.121
$\text{Fe}_A\text{-O}$ (1st shell)	4.0	0.007	1.948
$\text{Fe}_B\text{-Fe}_B$ (2nd shell)	4.9	0.012	3.024
$\text{Fe}_A\text{-Fe}_B$ (2nd shell)	1.1	0.012	3.546
$\text{Fe}_A\text{-Fe}_A$ (2nd shell)	4	0.011	3.486
$\text{Fe}_A\text{-Li}_B$ (2nd shell)	12	0.040	3.143

$S_0^2 = 1.0$, $\Delta E_0 = 2.143$ eV, $x^* = 0.886 \pm 0.02$, $(1-x)^{**} = 0.114 \pm 0.02$

N is the coordination number; $\text{Fe}_B\text{-O}$, $\text{Fe}_A\text{-O}$, $\text{Fe}_B\text{-Fe}_B$, $\text{Fe}_A\text{-Fe}_B$, $\text{Fe}_A\text{-Fe}_A$, $\text{Fe}_A\text{-Li}_B$ are the respective average interatomic distances and mean-square relative displacement σ^2 . The overall reduction factor S_0^2 is fixed at 1.00

* x here is the Weight% of $\text{Fe}_A\text{-O}$ bonds in the Fe–O spectrum component

(1- x) ** is the contribution% of $\text{Fe}_B\text{-O}$ bonds in the XANS spectrum

composite by changing the distribution of the magnetic ions, their spin orientation particularly at interfaces region, and consequently affecting the magnetic interactions [28–30].

The room temperature M–H hysteresis loops of $(x)\text{BTO}/(1-x)\text{LFO}$ ($x = 0.0, 0.2, 0.4, 0.6, 0.8$), are shown in Fig. 11. It is found that, the nanocomposites exhibit magnetic hysteresis curves, indicating that the nanocomposites are in ferrimagnetic ordering, arisen from Li-ferrite phase. The origin of the magnetic

properties was influenced by the cation distribution (within the magnetic phase), that was calculated and extracted from the EXAFS data analysis and fitting, respectively. It is widely accepted that the inclusion of Li^+ and extra Fe^{3+} in the lattice parameters, the cation arrangement between the tetrahedral and octahedral sites leads to that decreases the M_s to rather low values.

Figure 12a illustrates the dependence of the coercivity (H_C) and the saturation magnetization (M_s) on

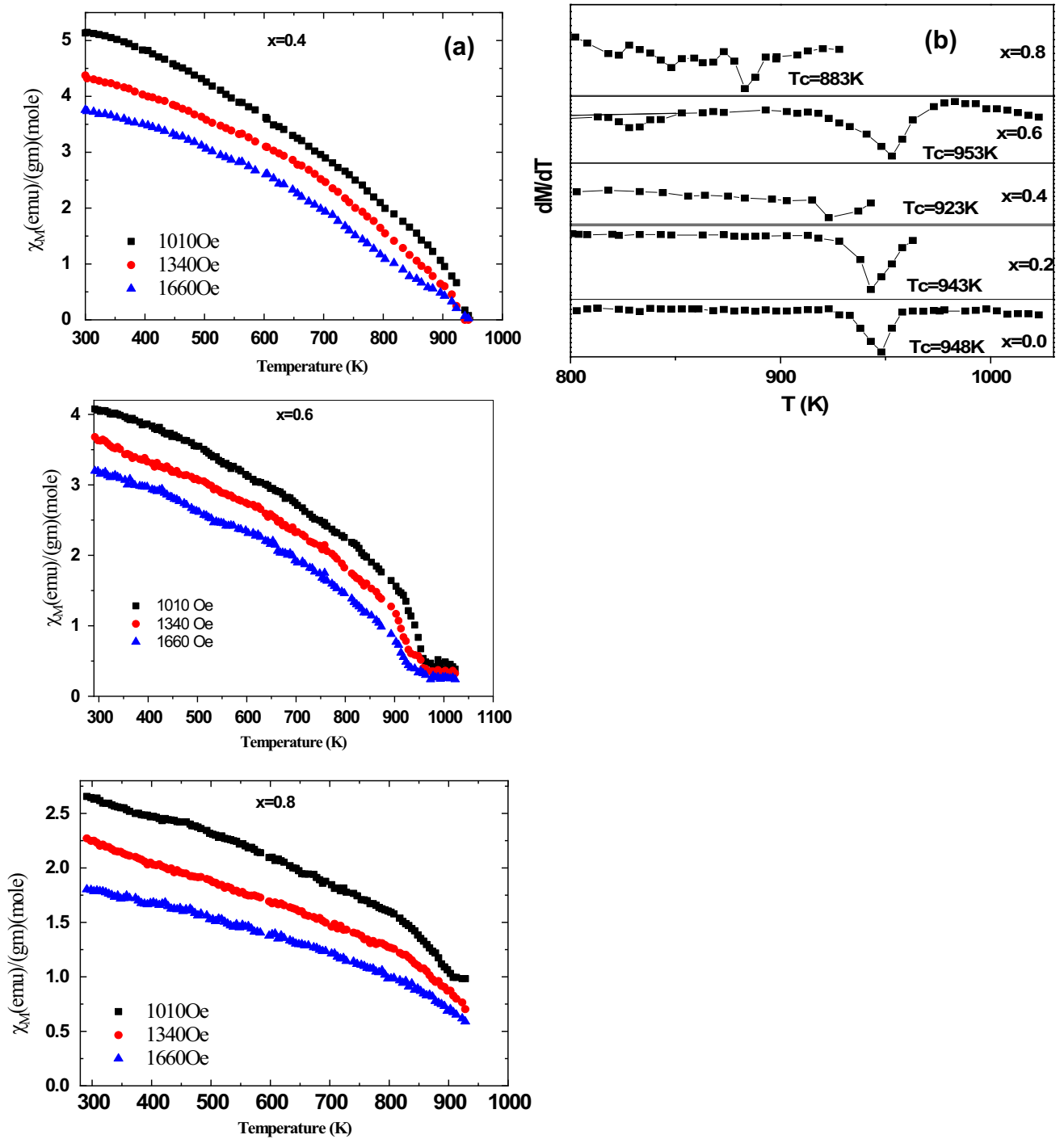


Fig. 9 a Effect of temperature on the molar magnetic susceptibility (χ_M) for (x) BTO/ $(1 - x)$ LFO; with $0.0 \leq x \leq 0.8$ nanocomposites. b First derivative of magnetization versus temperature to calculate T_C at different BTO concentration

BaTiO₃ content (x). It is clearly indicated that, the saturation magnetization of the magnetoelectric nanocomposite decreases linearly with increasing BTO content which may be caused by the existence of diamagnetic (BTO) phase along with the LFO phase.

Also, Fig. 12b along with Table 4 show the variation of the remanence ratio (M_r/M_s) with the BTO content, which expresses the squareness of the hysteresis loop. From Table 4, it is obvious also that H_C increases with the increase in BTO content (x).

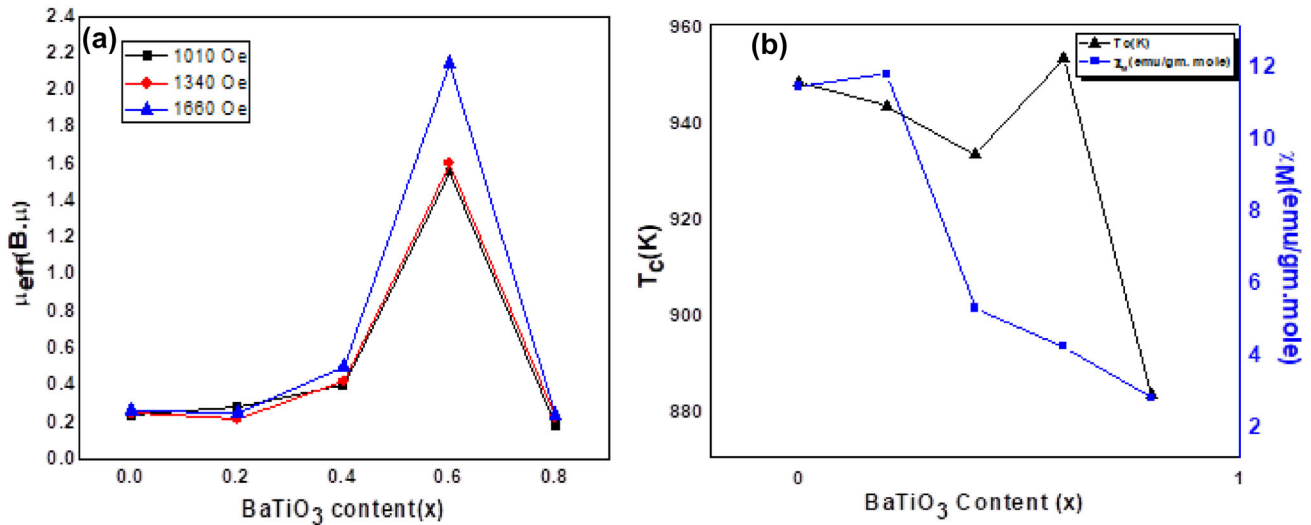


Fig. 10 **a** Effect of BaTiO₃ content (x) on the effective magnetic moment (μ_{eff}), **b** Effect of BaTiO₃ content (x) on T_C (K) and χ_M at room temperature

Table 3 Variation of the effective magnetic moment (μ_{eff}), Curie temperature (T_C), and χ_M at room temperature (RT) at different BTO (x) content for $(x)\text{BTO}/(1-x)\text{LFO}$; $x = 0.0, 0.2, 0.4, 0.6$, and 0.8 nanocomposite

x	μ_{eff} (BM)			T_C (K)	χ_M (RT)
	1010 Oe	1340 Oe	1660 Oe		
0	0.26	0.21	0.37	948	11.27
0.2	0.38	0.45	0.5	843	11.61
0.4	0.44	0.53	0.62	923	5.13
0.6	1.56	1.67	2.15	953	4.08
0.8	0.23	0.12	0.39	883	2.65

Furthermore, the saturation magnetization M_s plays a role in the behavior of H_C according to Brown's relation [31] which is given by; $H_C \geq (2K_1/\mu_0 M_s)$, where K_1 is the anisotropy constant, μ_0 is the permeability, M_s is the saturation magnetization. According to Brown's relation, H_C is inversely proportional to M_s which is obeyed the experimental data.

It is reported that the linear decrease in the magnetization of the composite with increasing x is simply due to the NON-MAGNETIC dilution of the magnetic material [32]. In this case, the average magnetization of the composite decreases linearly with increasing x . Similarly, a slight increase in the coercive force can be explained by the decrease in the magnetic interaction between the ferrite particles with an increase in the ratio of the non-magnetic component. Coercivity increased to rather high values; the sample with $x = 0.0$ has a value of 128.8 Oe while all the samples up to $x = 0.8$ have a coercivity of ≈ 143 Oe. It is clear that the structure disorder discovered from the EXAFS data analysis affected the observed magnetic behavior of the LFO phase, which in turns controlled the magnetic functionality of the BTO/LFO multiferroic nanocomposite.

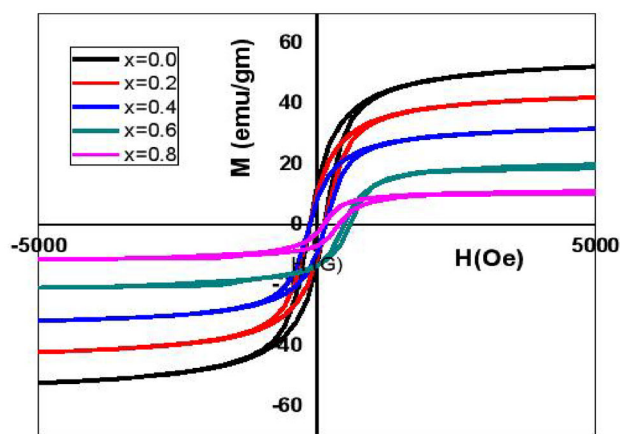


Fig. 11 Hysteresis loops for $(x)\text{BTO}/(1-x)\text{LFO}$; $0.0 \leq x \leq 0.8$ nanocomposites

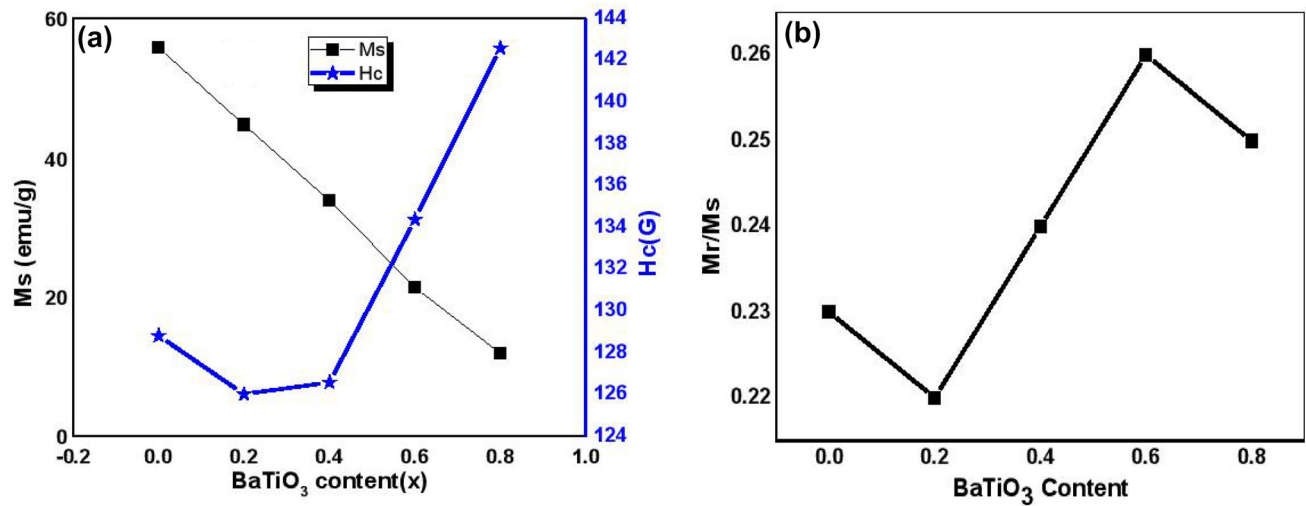


Fig. 12 a Influence of BaTiO_3 content on the magnetization parameters, b Variation of the ratio M_r/M_s at different BaTiO_3 content

Table 4 Magnetization parameters; M_s , M_r , H_C , and M_r/M_s for (x) BTO/(1 - x)LFO; x = 0.0, 0.2, 0.4, 0.6, 0.8 nanocomposites

x	M_s (emu/g)	M_r (emu/g)	H_C (G)	M_r/M_s
0	55.78	12.88	128.8	0.23
0.2	44.73	10.04	126	0.22
0.4	33.8	8.26	126.57	0.24
0.6	21.37	5.55	134.36	0.26
0.8	11.84	2.98	142.57	0.25

4 Conclusions

This research paper displays the results of the study of the two-phasic composite, (x) BaTiO_3 /(1 - x) $\text{Li}_{0.5}\text{Fe}_{2.5}\text{O}_4$, that was successfully constructed by modified sol-gel auto combustion method at relatively low temperature. Various advanced imaging and characterization techniques were used to study the structural, morphological, and magnetic properties of the synthesized composites: XRD, FTIR, XAFS, HRTEM, AFM and VSM. Interesting results were extracted from the XAFS measurements around Fe K-edge. The reflection of the structure analysis on the magnetic properties was studied and correlated. Modified citrate auto combustion was successful method for obtaining BaTiO_3 in nanorods-like shape. Tetra-*n*-butyl titanate was succeeded in preparing the single phase of BTO nanorods at a relatively low temperature. BaTiO_3 improved both $T_C = 953$ K and $H_C = 134.36$ G of the composite particularly at $x = 0.6$. XAFS results around Fe K-edge confirmed the

successful incorporation of the Li atoms into LFO lattice sites. The XANES fingerprint indicated that the Fe ions have a trivalent oxidation character (Fe^{3+}). The structure disorder discovered from the EXAFS data fit explained the observed magnetic behavior of the nanocomposite. The local atomic structure and the cation distribution of the magnetic phase were affecting strongly the observed magnetic performance of the BTO/LFO nanocomposite. Finally, the coupling between the perovskite (BaTiO_3) and the spinel ($\text{Li}_{0.5}\text{Fe}_{2.5}\text{O}_4$) phases forming the target multi-ferroic nanocomposite exerts the shared benefits of the two constituent phases in producing, novel, and more efficient advanced applications particularly in the energy saving field.

Acknowledgements

Access to Synchrotron radiation facilities of Elettra (beamline ‘XAFS’) is appreciated. The Synchrotron XAFS experiment has been supported by 11.1 XAFS Beamline @ Elettra Synchrotron at Trieste (Italy) through SESAME- IAEA-ICTP-Elettra program. The authors appreciate ICTP, IAEA, and EAEA. Neama Imam acknowledges deeply Giuliana Aquilanti, the head of XAFS and XRF beamlines at Elettra and her great group; Luca Olivi, Simone Pollastri, Danilo Oliveiradesouza, and Ilaria Carlomagno. Finally, we all pray for the memory and soul of the late professor M. A. Ahmed.

Author contributions

All authors have contributed, discussed the results and approved the final manuscript.

Funding

Open access funding provided by The Science, Technology & The author, N.G. Imam acknowledges the support provided from SESAME- IAEA-ICTP-Elettra program for XAFS measurements.

Data availability

The authors confirm that the data supporting the findings of this study are available within the article. However, the original collected Data are available by contacting the corresponding author. Also, the IFEFIT code used during the study are available online in accordance with funder data retention policies (the authors provide full citations that include URLs or DOIs.)

Declarations

Conflict of interest The authors declare that they have no known competing financial interests or personal relationships that could have appeared to influence the work reported in this work.

Open Access This article is licensed under a Creative Commons Attribution 4.0 International License, which permits use, sharing, adaptation, distribution and reproduction in any medium or format, as long as you give appropriate credit to the original author(s) and the source, provide a link to the Creative Commons licence, and indicate if changes were made. The images or other third party material in this article are included in the article's Creative Commons licence, unless indicated otherwise in a credit line to the material. If material is not included in the article's Creative Commons licence and your intended use is not permitted by statutory regulation or exceeds the permitted use, you will need to obtain permission directly from the copyright holder. To view a copy of this licence, visit <http://creativecommons.org/licenses/by/4.0/>.

References

1. K. Khan, A.K. Tareen, M. Aslam, R.U.R. Sagar, B. Zhang, W. Huang, A. Mahmood, N. Mahmood, K. Khan, H. Zhang, Z. Guo, Recent progress, challenges, and prospects in two-dimensional photo-catalyst materials and environmental remediation. *Nano-Micro Lett.* **12**, 167 (2020). <https://doi.org/10.1007/s40820-020-00504-3>
2. N.G. Imam, M. AbouHasswa, N. Okasha, Synchrotron X-ray absorption fine structure study and dielectric performance of $\text{Li}_{0.5}\text{Fe}_{2.5}\text{O}_4/\text{BaTiO}_3$ multiferroic. *J. Mater. Sci.: Mater. Electron.* **32**, 21492–21510 (2021). <https://doi.org/10.1007/s10854-021-06658-z>
3. N.V. Srihari, K.B. Vinayakumar, K.K. Nagaraja, Magneto-electric coupling in bismuth ferrite-challenges and perspectives. *Coatings* **10**, 1221 (2020). <https://doi.org/10.3390/coatings10121221>
4. M.S. Huzan, M. Fix, M. Aramini, P. Bencok, J.F. Mosselmans, S. Hayama, F.A. Breitner, L.B. Gee, C.J. Titus, M.A. Arrio, A. Jesche, M.L. Baker, Single-ion magnetism in the extended solid-state: insights from X-ray absorption and emission spectroscopy. *Chem. Sci.* **11**, 11801 (2020). <https://doi.org/10.1039/d0sc03787g>
5. H. Zeng, T. Tao, Y. Wu, W. Qi, C. Kuang, S. Zhou, Y. Chen, Lithium ferrite ($\text{Li}_{0.5}\text{Fe}_{2.5}\text{O}_4$) nanoparticles as anodes for lithium-ion batteries. *RSC Adv.* **4**, 23145 (2014). <https://doi.org/10.1039/c4ra02957g>
6. Y.-P. Fu, Electrical conductivity and magnetic properties of $\text{Li}_{0.5}\text{Fe}_{2.5-x}\text{Cr}_x\text{O}_4$ ferrite. *Mater. Chem. Phys.* **115**, 334–338 (2009). <https://doi.org/10.1016/j.matchemphys.2008.12.023>
7. J. Massoudi, D. Bouekkeze, A. Bougoffa, K. Khirouni, E. Dhahri, L. Bessais, Structural, elastic, optical and dielectric properties of $\text{Li}_{0.5}\text{Fe}_{2.5}\text{O}_4$ nanopowders with different particle sizes. *Adv. Powder Technol.* **31**(12), 4714–4730 (2020). <https://doi.org/10.1016/j.apt.2020.11.005>
8. X.Y. Zheng, L.J. Riddiford, J.J. Wisser, S. Emori, Y. Suzuki, Ultra-low magnetic damping in epitaxial $\text{Li}_{0.5}\text{Fe}_{2.5}\text{O}_4$ thin films. *Appl. Phys. Lett.* **117**, 092407 (2020). <https://doi.org/10.1063/5.0023077>
9. T. Amrillah, A. Hermawan, C.P. Wulandari, A.D. Muthi'Ah, F.M. Simanjuntak, Crafting the multiferroic BiFeO_3 - CoFe_2O_4 nanocomposite for next-generation devices: a review. *Mater. Manuf. Processes* (2021). <https://doi.org/10.1080/10426914.2021.1945096>
10. C.M. Costa, K.J. Merazzo, R. Gonçalves, C. Amos, S. Lancers-Méndez, Magnetically active lithium-ion batteries towards battery performance improvement. *iScience* **24**(6), 102691 (2021). <https://doi.org/10.1016/j.isci.2021.102691>
11. A.I. Ali, C.W. Ahn, Y.S. Kim, Enhancement of piezoelectric and ferroelectric properties of BaTiO_3 ceramics by aluminium

- doping. *Ceram. Int.* **39**(6), 6623–6629 (2013). <https://doi.org/10.1016/j.ceramint.2013.01.099>
12. A.I. Ali, A. Ullah, K. Park, R. Huh, Y.S. Kim, Ferroelectric enhancement of La-doped BaTiO₃ thin films using SrTiO₃ buffer layer. *Thin Solid Films* **551**, 127–130 (2014). <https://doi.org/10.1016/j.tsf.2013.11.048>
 13. N.G. Imam, M. AbouHasswa, G. Aquilanti, S.I. El Dek, N. Okasha, A.A.G. Al Shahawy, Influence of polyethylene glycol on the physical properties of Co_{0.2}Fe_{2.8}O₄ nanoparticles used as MRI contrast agent; synchrotron radiation Fe K-edge XAFS. *J. Mater. Res. Technol.* (2021). <https://doi.org/10.1016/j.jmrt.2021.09.143>
 14. E.G. Zaki, N.G. Imam, *Synchrotron Radiation in Petroleum Applications* (Lambert Academic Publishing, Saarbrücken, 2017)
 15. N.G. Imam, G. Aquilanti, A.A. Azab, S.E. Ali, Correlation between structural asymmetry and magnetization in Bi-doped LaFeO₃ perovskite: a combined XRD and synchrotron radiation XAS study. *J. Mater. Sci.: Mater. Electron.* **32**, 3361–3376 (2021). <https://doi.org/10.1007/s10854-020-05084>
 16. M.M. Arman, N.G. Imam, R.L. Portales, S.I. El-Dek, Synchrotron radiation X-ray absorption fine structure and magnetization improvement of A-site Ce³⁺ doped LaFeO₃. *J. Magn. Magn. Mater.* **513**, 167097 (2020). <https://doi.org/10.1016/j.jmmm.2020.167097>
 17. N. George, J.K. Thomas, H.P. Kumar, M.K. Suresh, V.R. Kumar, P.R.S. Wariar, R. Josed, J. Koshya, Characterization, sintering and dielectric properties of nanocrystalline barium titanate synthesized through a modified combustion process. *Mater. Charact.* **60**, 322 (2009). <https://doi.org/10.1016/j.materchar.2008.09.012>
 18. M.P. Pileni, Magnetic fluids: fabrication, magnetic properties, and organization of nanocrystals. *Adv. Funct. Mater.* **11**, 323 (2001). [https://doi.org/10.1002/1616-3028\(200110\)11:5%3c323::AID-ADFM323%3e3.0.CO;2-J](https://doi.org/10.1002/1616-3028(200110)11:5%3c323::AID-ADFM323%3e3.0.CO;2-J)
 19. M.A. Ahmed, N. Okasha, N.G. Imam, Advanced imaging techniques for characterization of 0.5BaTiO₃/0.5Ni_{0.5}Zn_{0.5}Fe₂O₄ multiferroic nanocomposite. *J. Alloys Compd.* **557**, 130 (2013). <https://doi.org/10.1016/j.jallcom.2012.12.036>
 20. M.A. Zayed, M.A. Ahmed, N.G. Imam, D.H. El Sherbiny, Analytical characterization of hematite/magnetite ferrofluid nanocomposites for hyperthermia purposes. *J. Supercond. Nov. Magn.* **29**, 2899–2916 (2016). <https://doi.org/10.1007/s10948-016-3587>
 21. B.H. Tchuioua, B.T. Sendja, J.M. Mane, G. Aquilanti, J.R. Plaisier, EXAFS study of the temperature dependence of the Debye-Waller factor in ZnSe zincblende compound. *Phys. Scr.* **95**, 045704 (2020). <https://doi.org/10.1088/1402-4896/ab6795>
 22. B. Ravel, M. Newville, A. Athena, Hephaestus: data analysis for X-ray absorption spectroscopy using IFEFFIT. *J. Synchrotron Radiat.* **12**, 537–541 (2005). <https://doi.org/10.1107/S0909049505012719>
 23. J.J. Rehr, R.C. Albers, Theoretical approaches to x-ray absorption fine structure. *Rev. Mod. Phys.* **72**, 621 (2000). <https://doi.org/10.1103/RevModPhys.72.621>
 24. A.A.H. El-Bassuony, A comparative study of physical properties of Er and Yb nanophase ferrite for industrial application. *J. Supercond. Nov. Magn.* (2018). <https://doi.org/10.1007/s10948-017-4543-1>
 25. D. Carta, G. Mountjoy, G. Navarra, M.F. Casula, D. Loche, S. Marras, A. Corrias, X-ray absorption investigation of the formation of cobalt ferrite nanoparticles in an aerogel silica matrix. *J. Phys. Chem. C* **111**, 6308–6317 (2007). <https://doi.org/10.1021/jp0708805>
 26. K.K. Kefeni, B.B. Mamba, T.A.M. Msagati, Application of spinel ferrite nanoparticles in water and wastewater treatment: a review. *Sep. Purif. Technol.* **188**, 399–422 (2017). <https://doi.org/10.1016/j.seppur.2017.07.015>
 27. R.R. Chilwar, A.R. Chavan, M.K. Babrekar, K.M. Jadhav, Impact of trivalent metal ion substitution on structural, optical, magnetic and dielectric properties of Li_{0.5}Fe_{2.5}O₄ thin films. *Physica B* **566**, 43–49 (2019). <https://doi.org/10.1016/j.physb.2019.04.031>
 28. M. Coduri, P. Masala, L. Del Bianco, F. Spizzo, D. Ceresoli, C. Castellano, S. Cappelli, C. Oliva, S. Checchia, M. Allieta, D.-V. Szabo, S. Schlabach, M. Hagelstein, C. Ferrero, M. Scavini, Local structure and magnetism of Fe₂O₃ maghemite nanocrystals: the role of crystal mansion. *Nanomaterials* **10**, 867 (2020). <https://doi.org/10.3390/nano10050867>
 29. M.A. Ahmed, N.G. Imam, M.K. Abdelmaksoud, Y.A. Saeid, Magnetic transitions and butterfly-shaped hysteresis of Sm-Fe-Al-based perovskite-type orthoferrite. *J. Rare Earth* **33**, 965 (2015). [https://doi.org/10.1016/S1002-0721\(14\)60513-5](https://doi.org/10.1016/S1002-0721(14)60513-5)
 30. M. Joung, J. Kim, M. Song, J. Choi, S. Nahm, C. Choi, T. Sung, Synthesis of highly tetragonal BaTiO₃ nanopowders by a two-step alkoxide–hydroxide route. *J. Alloys Compd.* **509**, 9089–9092 (2011). <https://doi.org/10.1016/j.jallcom.2011.06.052>
 31. A.M. Abo El Ataa, S.M. Attia, D. El Konya, A.H. Al-Hammadi, Spectral, initial magnetic permeability and transport studies of Li_{0.5–0.5x}Co_xFe_{2.5–0.5x}O₄ spinel ferrite. *J. Magn. Magn. Mater.* **295**(1), 28–36 (2005). <https://doi.org/10.1016/j.jmmm.2004.12.035>
 32. S.F. Mansour, N.G. Imam, S. Goda, M.A. Abdo, Constructive coupling between BiFeO₃ and CoFe₂O₄; promising magnetic and dielectric properties. *Mater. Res. Technol.* **9**(2), 1434–1446 (2019). <https://doi.org/10.1016/j.jmrt.2019.11.069>

Publisher's Note Springer Nature remains neutral with regard to jurisdictional claims in published maps and institutional affiliations.